

Long-range magnetic order in $\text{Fe}_3\text{O}_4/\text{NiO}$ superlattices

J. A. Borchers and R. W. Erwin

Reactor Radiation Division, National Institute of Standards and Technology, Gaithersburg, Maryland 20899

S. D. Berry and D. M. Lind

Department of Physics and the Center for Materials Research and Technology, Florida State University, Tallahassee, Florida 32306

J. F. Ankner

Research Reactor Facility, University of Missouri, Columbia, Missouri 65211

E. Lochner, K. A. Shaw, and D. Hilton

Department of Physics and the Center for Materials Research and Technology, Florida State University, Tallahassee, Florida 32306

(Received 15 July 1994)

Using neutron diffraction, x-ray scattering, and bulk-magnetization methods, we have characterized the magnetic structure for $\text{Fe}_3\text{O}_4/\text{NiO}$ superlattices grown by molecular-beam epitaxy. The antiferromagnetic NiO order extends through several superlattice bilayers, even though the intervening Fe_3O_4 layers are ferrimagnetic. The structural and magnetic coherence of the Fe_3O_4 is limited by interfacial stacking faults between adjacent layers resulting from symmetry differences between the NiO rocksalt and Fe_3O_4 spinel unit cell. The diffraction data manifest this interfacial disorder via a broadening of selected reflections. Using a structure-factor model based upon a Hendricks-Teller description of the random-stacking sequence, we have separated the magnetic order parameters of the Fe_3O_4 and NiO interlayers. The NiO appears to order at temperatures larger than T_N for bulk (520 K) due to coupling to the Fe_3O_4 layers ($T_C = 858$ K). The dependence of this enhancement on the relative NiO composition is qualitatively consistent with the predictions of mean-field theory.

I. INTRODUCTION

As an extension of recent efforts focusing on the magnetic properties of metallic superlattices,¹ interest has emerged in superlattices composed of antiferromagnetic insulators and related compounds, such as $\text{FeF}_2/\text{MnF}_2$,² NiO/CoO ,^{3,4} and $\text{Fe}_3\text{O}_4/\text{NiO}$.⁵⁻⁸ Compared with their metallic counterparts, the understanding of these materials is straightforward from a theoretical perspective⁹⁻¹² because the moments are localized and the spin interactions are short range. Difficulty arises, however, in the determination of the magnetic structure using standard bulk magnetization methods. Instead, elastic neutron diffraction provides a direct measure of the temperature-dependent moment in these superlattices,^{6-8,13} supplementing characterization by inferential techniques such as thermal expansion² and exchange anisotropy.¹⁴ For example, NiO/CoO superlattices,^{3,4} studied by neutron diffraction, exhibit anomalous magnetic behavior near the phase transition due to differences between the Néel temperatures of the bulk constituents.

In this study Fe_3O_4 and NiO were chosen as superlattice components due to their disparate magnetic ordering temperatures, as well as their contrasting magnetic structures. Below $T_N = 520$ K the $1.9\mu_B$ spins in bulk NiO order in ferromagnetic sheets that are coupled antiferromagnetically along the [111] direction through

the rocksalt crystalline lattice.¹⁵ Bulk Fe_3O_4 crystallizes in the inverse spinel structure with trivalent and divalent Fe ions, possessing moments of $5.0\mu_B$ and $4.2\mu_B$, respectively, distributed among inequivalent tetrahedral and octahedral sites. Below $T_C = 858$ K the resultant magnetic structure is ferrimagnetic with a net moment of $4.2\mu_B$ per unit cell.¹⁶ The structural, magnetic and electronic characteristics of bulk Fe_3O_4 change abruptly at 118 K, the Verwey transition. Cooling through this temperature, the easy axis of magnetization switches from the [111] to the [001] direction as the lattice undergoes a rhombohedral distortion.¹⁷

As expected, the magnetic properties of the composite superlattices reflect those of the Fe_3O_4 and NiO constituents. Exploiting intrinsic differences between the symmetry of the spinel and rocksalt lattices, we have characterized the magnetic order in the NiO and Fe_3O_4 layers using neutron diffraction methods.⁶⁻⁸ At low temperatures the NiO antiferromagnetic order propagates coherently through several superlattice bilayers. The Fe_3O_4 ferrimagnetic order, however, is confined to individual interlayers in samples with NiO layer thicknesses exceeding 15 \AA , due to random stacking of the spinel unit cell at the interfaces. A model for the diffraction data, incorporating a Hendricks-Teller description¹⁸ of these stacking faults, accounts for qualitative differences among the measured line shapes of selected structural and magnetic reflections. Within the framework of the

model, we have extracted the magnetic order parameters of the NiO and Fe_3O_4 components from measurements of the temperature-dependent (111) peak. Specifically, the Néel temperature of NiO appears to shift upward toward that of bulk Fe_3O_4 as the compositional fraction of NiO in each interlayer is decreased. This scaling behavior can be understood within the context of a mean-field theory^{3,9-11} developed to describe Ising-like antiferromagnetic superlattices. Details of these magnetic and structural properties, obtained using x-ray scattering, neutron diffraction, and SQUID magnetometry, are presented in the following sections.

II. PREPARATION AND STRUCTURAL CHARACTERIZATION

The $\text{Fe}_3\text{O}_4/\text{NiO}$ superlattices considered in this study were grown using oxygen plasma-assisted molecular-beam epitaxy (MBE). In this process, high-purity Fe and Ni metals are evaporated from electron-beam hearths onto a 1-in.-diam MgO substrate in a controlled oxygen flux provided by an electron cyclotron resonance microwave ionization source. The flux rates of the metals and oxygen are optimized and stabilized during growth to produce the desired stoichiometries. The deposition is monitored by reflection high-energy electron diffraction (RHEED) to ensure crystalline layer-by-layer growth. As expected, the NiO and Fe_3O_4 layers retain the [001] orientation of the underlying MgO. The implementation of this MBE procedure is outlined elsewhere.⁵

Five superlattices were prepared for the neutron diffraction experiments with the bilayer repeat distance held constant near 100 Å and the relative thicknesses of the Fe_3O_4 and NiO interlayers varied. For comparison we also have examined 1 μm thick NiO and 3 μm thick Fe_3O_4 films. Overall the qualitative structural characteristics of these samples, determined using x-ray diffraction techniques, are consistent with those obtained for a similar series of superlattices.^{5,7,8} Most of the x-ray diffraction measurements presented here were performed on a double-axis diffractometer with Cu $K\alpha$ radiation from a fixed-anode source. Scans along the growth direction and along symmetry directions tilted away from the film normal confirm the growth of single-phase, crystalline layers that are lattice matched at the interfaces despite the 0.6% difference between the NiO-rocksalt and Fe_3O_4 -spinel unit cells ($a = 8.352$ and 8.398 Å, respectively).

Figure 1 shows one such scan along the growth axis through the (004) reflection¹⁹ for $[\text{Fe}_3\text{O}_4(34 \text{ \AA})|\text{NiO}(68 \text{ \AA})]_{300}$, a superlattice comprising 300 bilayers with 34 Å of Fe_3O_4 and 68 Å of NiO. The rocking curve widths of the first- and second-order superlattice reflections vary from $0.4 \pm 0.1^\circ$ for $[\text{Fe}_3\text{O}_4(34 \text{ \AA})|\text{NiO}(68 \text{ \AA})]_{300}$ to $1.0 \pm 0.15^\circ$ for $[\text{Fe}_3\text{O}_4(67 \text{ \AA})|\text{NiO}(33 \text{ \AA})]_{400}$, which is somewhat larger than the $0.03 \pm 0.01^\circ$ mosaic of the MgO substrate. The broadening may reflect a gradual degradation of the structural quality in the topmost layers. In Fig. 1 superlattice sidebands are evident up to seventh order suggesting that the concentration and strain gradients through the interfaces are abrupt.

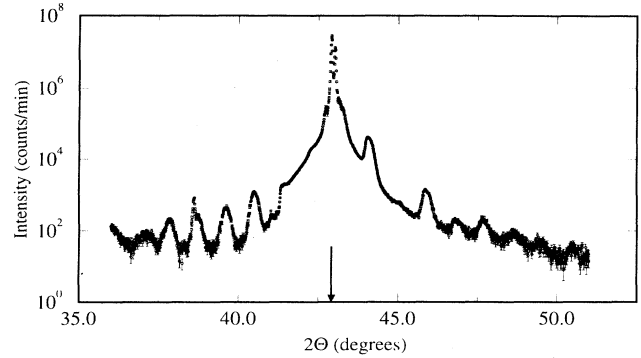


FIG. 1. Room-temperature x-ray diffraction scan along the growth-axis direction through the (004) reflection for $[\text{Fe}_3\text{O}_4(34 \text{ \AA})|\text{NiO}(68 \text{ \AA})]_{300}$. The MgO substrate peak is marked with an arrow.

Because the central Bragg reflection is partially obscured by the MgO substrate peak, it is difficult to obtain precise structural characteristics of the sample from the high-angle diffraction data. After careful subtraction of the MgO scattering, we are continuing efforts to fit these and similar data for related samples⁵⁻⁸ using kinematic models for imperfect superlattices.^{20,21} The substrate interference, however, is completely eliminated at low angles, where the scattered intensity from the MgO appears as a featureless background. The specular reflectivity of $[\text{Fe}_3\text{O}_4(75 \text{ \AA})|\text{NiO}(9 \text{ \AA})]_{500}$ is shown in Fig. 2(a), plotted as a function of the wave vector $Q = 4\pi\sin\theta/\lambda$, where θ is the reflected angle measured with respect to the surface and λ is the wavelength of the x-ray beam (≈ 1.542 Å). The fitted curve is calculated from the profile of the scattering density Nb in Fig. 2(b), where N is the number density and b is the average atomic scattering amplitude of the layer. The refinement algorithm is based upon the solution of the one-dimensional wave equation for a stratified medium, which is detailed elsewhere.²² We have not included the effects of bilayer thickness fluctuations, which would account for the broadening of the superlattice reflections with increasing Q .²⁰ Though superlattice peaks are visible out to ninth order, our fit reveals that the 74.6 ± 1.0 Å thick Fe_3O_4 and 8.7 ± 1.0 Å thick NiO layers are smeared at the interfaces over $\gtrsim 10$ Å. Because reflectivity analysis is insensitive to the length scale of the in-plane structural correlations that give rise to the interlayer “mixing,” atomic-scale interdiffusion and roughness are indistinguishable from terraced interfaces with atomically pure layers. Qualitative information about the origin of the disorder can be gained from measurements of the diffuse background (i.e., off-specular reflectivity) which is large and has periodic features similar to those in the specular reflectivity [Fig. 2(a)]. These data suggest that the interfacial roughness is strongly correlated from one interface to the next²³ and that the layering is well-defined locally. The apparent diffuse character of the interface morphology probably originates from the $\approx 0.5^\circ$ miscut of the MgO substrate and incomplete atomic-layer filling during interface growth, rather than from interdiffusion or pinhole formation.

While specular reflectivity is invaluable for the determination of the concentration variation through the superlattice, it provides no information about the crystalline coherence or strain modulation. The lattice structure within the individual Fe_3O_4 layers can be isolated simply by measuring peaks forbidden by symmetry for the NiO and MgO. For example, the angular position of the (220) in-plane reflection for $[\text{Fe}_3\text{O}_4(75 \text{ \AA})|\text{NiO}(9 \text{ \AA})]_{500}$ indicates that the Fe_3O_4 layers are compressed $< 0.2\%$ to match the smaller NiO lattice. Detailed measurements of the (022), (026), and (066) reflections also reveal that the structural coherence of the Fe_3O_4 lattice is limited along the growth direction by stacking faults at the superlattice interfaces.^{6,7} During growth the oxygen sublattice, common to the Fe_3O_4 , NiO, and MgO, preserves the lattice orientation through the entire superlattice. Defects form at the interfaces, however, because the iron tetrahedral sites in the spinel unit cell have no analogue in the NiO rocksalt structure. Therefore, the Fe_3O_4 lattice does not maintain its registry across intervening NiO interlayers. For a comparable series of superlattices⁵ with 68 \AA Fe_3O_4 layers and thick NiO layers ($\approx 15 \text{ \AA}$), the actual coherence length along the [001] direction obtained from the full width at half maximum (FWHM) of the (026)

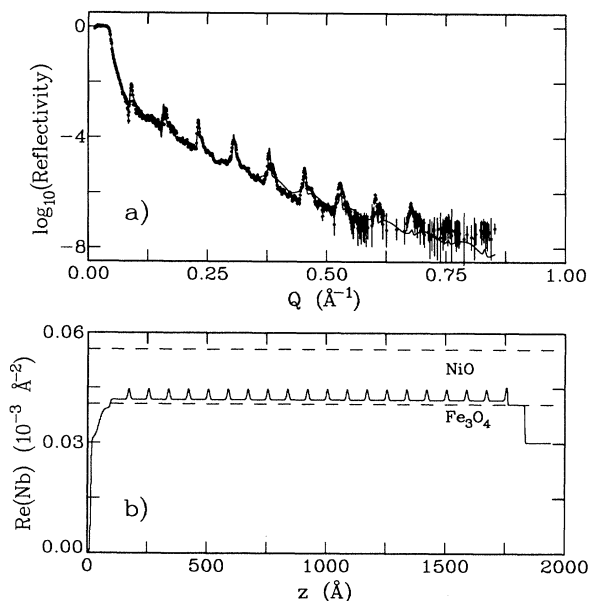


FIG. 2. (a) Specular x-ray reflectivity of $[\text{Fe}_3\text{O}_4(75 \text{ \AA})|\text{NiO}(9 \text{ \AA})]_{500}$ plotted as a function of the wave vector Q . The open circles are the data and the solid line corresponds to the fit. This fit was obtained for a superlattice with 100 bilayer repeats, rather than the actual 500, for computational efficiency. The diffuse background has been measured and subtracted from the data. (b) Scattering density profile extracted from the reflectivity fit. N is the number density of the material with scattering amplitude b . The dashed lines show the bulk densities of Fe_3O_4 and NiO, as marked. The profile is shown for a superlattice with 20 bilayer repeats, rather than 500, for clarity.

reflection is smaller than the superlattice repeat distance. This disorder is not evident for a sample with 68 \AA of Fe_3O_4 and 9 \AA of NiO, which has a coherence length exceeding 480 \AA . As has been demonstrated for $[\text{Fe}_3\text{O}_4(75 \text{ \AA})|\text{NiO}(9 \text{ \AA})]_{500}$ (Fig. 2), small amounts of Fe are probably present throughout the NiO interlayers in this sample.

III. NEUTRON DIFFRACTION PROCEDURES

Neutron scattering experiments, which yield information about both the crystalline and magnetic ordering in these superlattices, corroborate the results of the x-ray structural characterization. The neutron diffraction data were obtained on BT-9, a triple-axis spectrometer at the National Institute of Standards and Technology reactor. For these studies a pyrolytic graphite (PG) monochromator was set to select neutrons of wavelength 2.35 \AA incident upon the sample, and a PG analyzer was positioned for zero-energy transfer to reduce the inelastic background. A second triple-axis spectrometer, BT-2, was configured for polarized beam measurements by replacing the PG monochromator and analyzer with Heusler-alloy crystals, which preferentially scatter only one of the two neutron spin states. On both instruments, the samples were mounted in an Al holder on the cold finger of a closed-cycle refrigerator capable of regulating temperatures between 10 K and 475 K . Temperatures between 450 K and 675 K were attained using an evacuated furnace.

During these experiments the superlattices were aligned with the [004] surface normal and one of the two [220] film-plane axes in the scattering plane to allow access to the (222), (111), and (220) reflections. The schematic in Fig. 3 shows the orientation of these reflections relative to the sample surface in reciprocal space. Scans were performed along the scattering-vector direction and along the growth direction to probe the coherence of the spin propagation through the superlattice layers. Typically, collimation of $40'-48'-48'$ provided resolution better than 0.034 \AA^{-1} along the growth direction (z axis) and 0.035 \AA^{-1} along the wave vector (Q) direction.

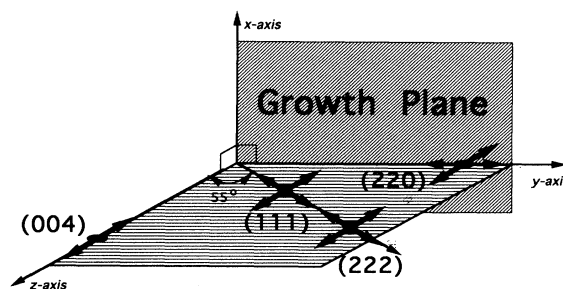


FIG. 3. Schematic showing the reciprocal space reflections discussed in the text. The scan directions through each peak are designated with arrows.

IV. STRUCTURE-FACTOR CALCULATION

It is well known that only growth-axis data are sensitive to the superlattice modulation. To extract the spatial variation of the crystalline and magnetic structure through the superlattice bilayers, we calculate the scattering cross section for the z -axis scans through the (222), (111), and (220) reflections. For these materials, both the nuclear and magnetic terms contribute to the scattered intensity as follows:

$$I(\mathbf{Q}) \propto \left| \sum_{\mathbf{r}} b_r e^{i\mathbf{Q}\cdot\mathbf{r}} \right|^2 + \left| \sum_{\mathbf{r}} p_r e^{i\mathbf{Q}\cdot\mathbf{r}} \right|^2, \quad (1)$$

where b_r is the nuclear scattering amplitude of the atom at position \mathbf{r} . The effective magnetic scattering amplitude is $p_r = \sigma_m f_r(\mathbf{Q}) |\mathbf{S}_{\perp r}|$, where $\sigma_m = 0.2695 \times 10^{-12}$ cm and $f_r(\mathbf{Q})$ is the magnetic form factor. The magnetic

moment at site r , $\mathbf{S}_{\perp r} = S_r [\hat{\mathbf{S}} - (\hat{\mathbf{S}} \cdot \hat{\mathbf{Q}}) \hat{\mathbf{Q}}]$, includes a geometrical factor that selects the component of the moment perpendicular to the scattering-vector direction.

We perform explicit lattice sums along the $[0\ 0\ l]$ (defined here as the z axis) and $[l\ l\ 0]$ (defined here as the y axis) directions to describe the reflections in the scattering plane shown in Fig. 3. For simplicity, we assume that the bilayer thickness Λ is uniform throughout the entire superlattice though the x-ray reflectivity data show evidence of slight bilayer thickness fluctuations [Fig. 2(a)]. The atomic positions can thus be expressed as $\mathbf{r}(k, m, n) = [k\Lambda + z(m, n)]\hat{\mathbf{z}} + y(m, n)\hat{\mathbf{y}}$ where k indexes the bilayer, $z(m, n)$ is the m th position along the z axis relative to the beginning of the bilayer and $y(m, n)$ is the n th position along the y axis relative to the origin. Specifically, $z(N_{\Lambda}, n) = \Lambda$ for a bilayer consisting of N_{Λ} atomic planes. Regrouping the structure factor in the usual manner,^{20,24} we write the nuclear intensity as

$$I_{\text{nuc}}(\mathbf{Q}) \propto \left| \sum_k^{N_{\text{tot}}} e^{ikQ_z\Lambda} \left| \sum_{m=1}^{N_{\Lambda}} \sum_n b(m, n) e^{iQ_z z(m, n) + iQ_y y(m, n)} \right|^2 \right|^2, \quad (2)$$

where N_{tot} is the total number of bilayers comprising the superlattice. The first factor produces a series of sharp peaks at $Q_z = k(2\pi/\Lambda)$, attenuated by the second factor which is the square of the structure factor $\mathcal{F}^{\text{nuc}}(\mathbf{Q})$ for a single bilayer. We note that the magnetic intensity can be expanded in a similar manner. At the Fe₃O₄/NiO interface, $b(m, n)$ and $z(m, n)$ vary abruptly if the superlattice is a perfect rectangle wave. Realistically, diffusion, step formation, and strain gradients occur through the interface region as discussed in Sec. II. To account for these imperfections, we use a damped rectangle-wave model for the superlattice,^{3,24} in which the Fourier components of the concentration and d -spacing rectangle waves are reduced by damping factors. The nuclear scattering amplitude, for example, is written

$$b(m, n) = C_{\text{NiO}}(m, \alpha) b_{\text{NiO}}(m, n) + [1 - C_{\text{NiO}}(m, \alpha)] b_{\text{Fe}_3\text{O}_4}(m, n), \quad (3)$$

where $C_{\text{NiO}}(m, \alpha)$ is the concentration modulation of the NiO through a bilayer, defined by Erwin *et al.*²⁴ as

$$C_{\text{NiO}}(m, \alpha) = \frac{N_{\text{NiO}}}{N_{\Lambda}} + \frac{1}{\pi} \sum_{j=1}^{\infty} e^{-\alpha j^2} \frac{1}{j} \times \left[\sin \left[\frac{2\pi j}{N_{\Lambda}} \left(m - \frac{1}{2} \right) \right] - \sin \left[\frac{2\pi j}{N_{\Lambda}} \left(m - \frac{1}{2} - N_{\text{NiO}} \right) \right] \right] \quad (4)$$

and where α is a damping factor.

In calculating $\mathcal{F}^{\text{nuc}}(\mathbf{Q})$ and $\mathcal{F}^{\text{mag}}(\mathbf{Q})$, one must consider not only the variation of the Fe₃O₄ and NiO concentrations through each bilayer, but also the composition of each atomic plane within the individual interlayers. Specifically, the nuclear structure factor for the 64-atom unit cell of bulk NiO (Ref. 15) reduces to the following in the y - z scattering plane (Fig. 3):

$$\mathcal{F}_{\text{NiO}}^{\text{nuc}}(\mathbf{Q}) = 4b_{\text{O}} \left[e^{iQ_z a/4} + e^{iQ_y a\sqrt{2}/8} \right] \left[1 + e^{iQ_z a/2} \right] \left[1 + e^{iQ_y a\sqrt{2}/4} \right] + 4b_{\text{Ni}} \left[1 + e^{iQ_z a/4 + iQ_y a\sqrt{2}/8} \right] \left[1 + e^{iQ_z a/2} \right] \left[1 + e^{iQ_y a\sqrt{2}/4} \right]. \quad (5)$$

The neutron scattering lengths for nickel and oxygen²⁵ are designated b_{Ni} and b_{O} , respectively, and the lattice parameter a for NiO equals 8.352 Å. The magnetic structure factor has a form similar to the nuclear:

$$\mathcal{F}_{\text{NiO}}^{\text{mag}}(\mathbf{Q}) = 4p_{\text{Ni}} \left[1 - e^{iQ_z a/4 + iQ_y a\sqrt{2}/8} \right] \left[1 - e^{iQ_z a/2} \right] \left[1 - e^{iQ_y a\sqrt{2}/4} \right], \quad (6)$$

where S_{Ni} , implicit in the magnetic scattering amplitude p_{Ni} , is equal to $1.9\mu_B$. The oxygen sublattice in Fe₃O₄ is identical to that of NiO, but the 56-atom spinel unit cell leads to a more complex expression for the nuclear structure factor,¹⁶

$$\begin{aligned} \mathcal{F}_{\text{Fe}_3\text{O}_4}^{\text{nuc}}(\mathbf{Q}) = & 4b_{\text{O}} \left[e^{iQ_z a/4} + e^{iQ_y a\sqrt{2}/8} \right] \left[1 + e^{iQ_z a/2} \right] \left[1 + e^{iQ_y a\sqrt{2}/4} \right] \\ & + 2b_{\text{Fe}} \left(\left[1 + e^{iQ_z a/2} \right] \left[1 + e^{iQ_y a\sqrt{2}/4} \right] + 2e^{iQ_z a/4 + iQ_y a\sqrt{2}/8} \left[e^{iQ_z a/2} + e^{iQ_y a\sqrt{2}/4} \right] \right) \\ & + 2b_{\text{Fe}} e^{iQ_z a/8 + iQ_y a\sqrt{2}/8} \left[1 + e^{iQ_z a/4} \right] \left[1 + e^{iQ_z a/2 + iQ_y a\sqrt{2}/4} \right], \end{aligned} \quad (7)$$

where b_{Fe} is the neutron scattering length for Fe (Ref. 25) and $a = 8.398 \text{ \AA}$ for Fe_3O_4 . The form of the magnetic structure factor is again comparable:

$$\begin{aligned} \mathcal{F}_{\text{Fe}_3\text{O}_4}^{\text{mag}}(\mathbf{Q}) = & 2p_{+3,+2} \left(\left[1 + e^{iQ_z a/2} \right] \left[1 + e^{iQ_y a\sqrt{2}/4} \right] + 2e^{iQ_z a/4 + iQ_y a\sqrt{2}/8} \left[e^{iQ_z a/2} + e^{iQ_y a\sqrt{2}/4} \right] \right) \\ & - 2p_{+3} e^{iQ_z a/8 + iQ_y a\sqrt{2}/8} \left[1 + e^{iQ_z a/4} \right] \left[1 + e^{iQ_z a/2 + iQ_y a\sqrt{2}/4} \right], \end{aligned} \quad (8)$$

with p_{+3} representing the magnetic scattering amplitude of the Fe^{+3} ions at the tetrahedral sites and $p_{+3,+2}$ corresponding to the average amplitude of the Fe^{+3} and Fe^{+2} ions at the octahedral sites. We note that $S_{\text{Fe}^{+3}} = 5.0\mu_B$ and $S_{\text{Fe}^{+3,+2}} = 4.6\mu_B$. Theoretical and experimental determinations of the magnetic form factor $f(\mathbf{Q})$ for both Fe^{+3} and Ni^{+2} are summarized by Bacon.²⁵

As a rough gauge for the superlattice diffraction data, we compute in Table I the relative intensities of the (222), (111), and (220) reflections for bulk Fe_3O_4 and NiO from the structure factor equations above. For simplicity, it is assumed that the moments in both materials are uniformly distributed among equivalent axial domains. Clearly, the (222) reflection is dominated by the NiO structural contribution. Scattering from the NiO antiferromagnetic order appears at the (111) position, simultaneous with scattering from the Fe_3O_4 ferrimagnetic order. The (220) reflection, forbidden for NiO, is comprised of contributions from both the magnetic and nuclear structures of Fe_3O_4 .

The next step is to incorporate the structure factors outlined in Eqs. (5)–(8) into the expressions for the scattered intensity from a superlattice [Eqs. (1) and (2)], while accounting for symmetry differences between the Fe_3O_4 and NiO lattices. Though the oxygen sublattice is identical in both materials, the tetrahedral Fe sites have no parallel in the NiO structure, as described in Sec. II. By symmetry arguments, there are eight possible ways for the spinel unit cell to orient itself relative to the rocksalt template at each NiO/ Fe_3O_4 interface. The number of unique positions is reduced to four when the superlattice is projected onto the y - z plane, as illustrated in Fig. 4. [Notice that these four orientations can be generated simply by seeding the spinel unit cell at the NiO/ Fe_3O_4 interface with one of the four z -axis planes labeled 1, 2, 3, or 4 in Fig. 4. Stacking faults result

when the eight atomic-layer sequence of the Fe_3O_4 unit cell described by Eqs. (7) and (8) is interrupted at subsequent interfaces.] The bilayer structure factor $\mathcal{F}_s^{\text{nuc}}(\mathbf{Q})$ with $s = 1 - 4$ can be calculated for each of these orientations simply by adjusting phase factors in Eqs. (7) and (8). We postulate that these four configurations are distributed randomly among the N_{tot} superlattice interfaces with a probability of P_s . Next we average over all possible stacking sequences using a formalism developed by Hendricks and Teller¹⁸ and generalized by Méring²⁶ and Kakinoki²⁷ for a finite number of disordered layers. Equation (2) for the nuclear intensity reduces to the following:

$$I_{\text{nuc}}(\mathbf{Q}) \propto \frac{\sin^2(N_{\text{tot}}Q_z\Lambda/2)}{\sin^2(Q_z\Lambda/2)} \left[|\langle \mathcal{F}^{\text{nuc}}(\mathbf{Q}) \rangle|^2 \right] \quad (9a)$$

$$+ N_{\text{tot}} \langle |\mathcal{F}^{\text{nuc}}(\mathbf{Q})|^2 \rangle - N_{\text{tot}} |\langle \mathcal{F}^{\text{nuc}}(\mathbf{Q}) \rangle|^2. \quad (9b)$$

In this expression,⁶ $\langle \mathcal{F}^{\text{nuc}}(\mathbf{Q}) \rangle = \sum_{s=1}^4 P_s \mathcal{F}_s^{\text{nuc}}(\mathbf{Q})$ is the average structure factor for a single bilayer. The first term in Eq. (9a) represents the coherent Bragg scattering from the average superlattice configuration, and the

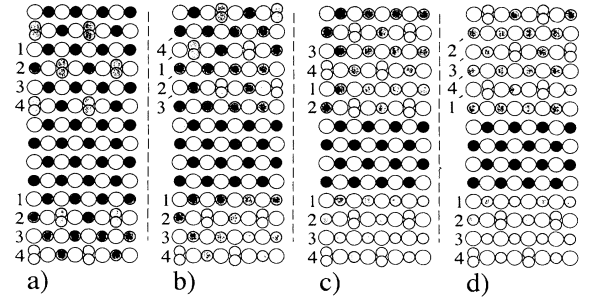


FIG. 4. Projection of a $\text{Fe}_3\text{O}_4/\text{NiO}$ interface in the y - z plane. Schematics (a)–(d) show the four possible orientations of the Fe_3O_4 -spinel lattice relative to the NiO-rocksalt lattice at each interface. (For clarity, the interfaces shown are not diffused or mixed, as may be the case in an actual superlattice.) The open circles represent the O^{+2} ions, the solid circles correspond to the Ni^{+2} ions, the shaded circles designate the Fe^{+2} and Fe^{+3} ions occupying the tetrahedral and octahedral sites. Symmetrically equivalent atomic planes in the spinel unit cell are numbered 1–4 in each interfacial configuration.

TABLE I. The relative nuclear and magnetic intensities for the reflections listed calculated for bulk Fe_3O_4 and NiO from the square of the structure factors given in Eqs. (5)–(8).

Index	Reflection		Fe_3O_4		NiO	
	Q_z	Q_y	Struc	Mag	Struc	Mag
(222)	$4\pi/a$	$4\sqrt{2}\pi/a$	10.9	91.6	207	0
(111)	$2\pi/a$	$2\sqrt{2}\pi/a$	5.00	145	0	58.9
(220)	0	$4\sqrt{2}\pi/a$	58.2	37.1	0	0

second (9b) is the incoherent scattering describing the deviation from the average configuration. Once again, a similar closed form can be written for the average magnetic intensity [second term of Eq. (1)].

The interfacial stacking-faults described by Eq. (9) lead to pronounced differences among the line shapes of the three reflections considered. As a demonstration, we apply the model to a hypothetical superlattice with 50 bilayers composed of 66.7 \AA of Fe_3O_4 and 33.2 \AA of NiO .²⁸ We require that diffusion is limited to $\approx 2 \text{ \AA}$ at the interfaces and that the components are lattice matched in the growth plane, but retain their bulk lattice spacings along the z -axis direction. With respect to the magnetic structure, we stipulate that the Fe and Ni moments are distributed uniformly among equivalent axial domains. Figure 5 shows Q_z scans through the (222), (111), and (220) peaks calculated assuming that the interfacial configurations in Fig. 4 occur with equal probability. The scattering at the (220) positions consists of a single broad peak with a FWHM of 0.085 \AA^{-1} . The corresponding coherence length of 78 \AA is roughly equal to the thickness

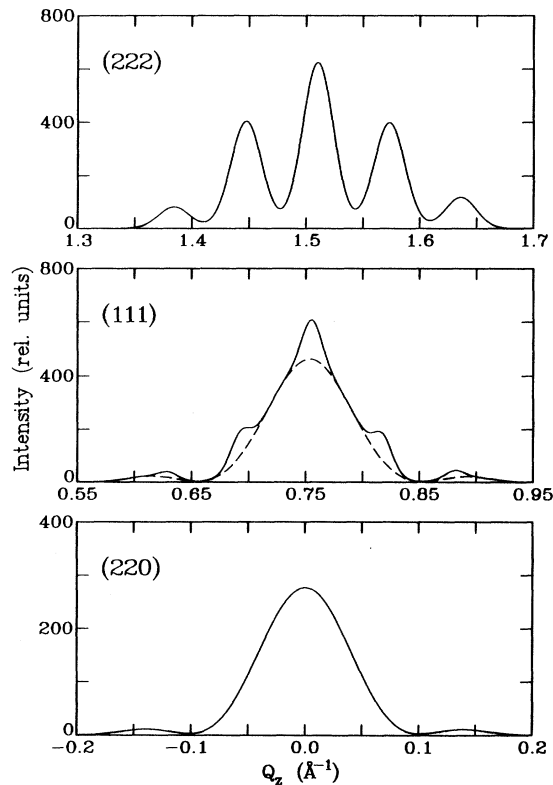


FIG. 5. Model calculations of Q_z scans through the (222), (111), and (220) reflections for a hypothetical superlattice $[\text{Fe}_3\text{O}_4(66.7 \text{ \AA})|\text{NiO}(33.2 \text{ \AA})]_{50}$ assuming that the four types of stacking faults described in the text occur with equal probability. The structure factor has been convoluted with a Gaussian resolution function (FWHM of 0.032, 0.019, and 0.028 \AA^{-1} , respectively) in order to simulate the experimental conditions. The dashed line in the (111) scan delineates the Fe_3O_4 scattering contribution (broad Gaussian) from that of the NiO (superlattice peaks).

of a Fe_3O_4 layer, confirming that this peak arises solely from the isolated Fe_3O_4 layers (Table I). In contrast, narrow superlattice peaks separated by $\Delta Q_z = \pm 0.063 \text{ \AA}^{-1}$ are evident in the (222) scan. The structure factors for each of the four lattice configurations in Fig. 4 differ by phase factors of 2π , rendering this peak insensitive to the type of stacking disorder prevalent in these superlattices. The (111) reflection, composed of a series of superlattice peaks superimposed on a Gaussian background, combines features of the (222) and (220). As demonstrated in Fig. 5, the broad peak results principally from the Fe_3O_4 , while the sharp components originate from the NiO antiferromagnetic order.

V. NEUTRON DIFFRACTION RESULTS

The qualitative characteristics of the neutron diffraction data for the $\text{Fe}_3\text{O}_4/\text{NiO}$ superlattices are consistent with the predictions of the structure-factor model. Figure 6 shows scans along the $[0 0 \ell]$ direction through the (222) reflection for four of the superlattices considered. In the scan for $[\text{Fe}_3\text{O}_4(75 \text{ \AA})|\text{NiO}(9 \text{ \AA})]_{500}$, superlattice sidebands are visible out to at least sixth order, but the central Bragg reflection is masked by scattering from the MgO substrate as it is in the high-angle x-ray scans (Fig. 1). Comparing the (222) data to the model calculation in Fig. 5, the relative intensities of the superlattice peaks are suggestive of sharp chemical interfaces. We also observe that these intensities do not vary with temperature. Polarized diffraction measurements for $[\text{Fe}_3\text{O}_4(75 \text{ \AA})|\text{NiO}(9 \text{ \AA})]_{500}$ verify that, as expected, the scattering is predominantly structural in character (Table I).

Scattering at the (220) position is highly sensitive to the structural stacking disorder between the Fe_3O_4

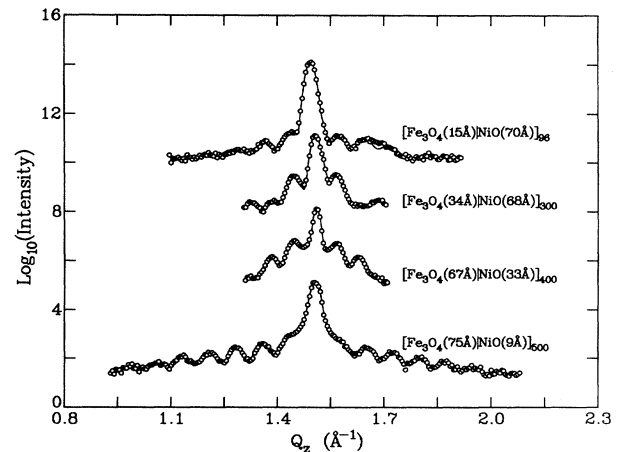


FIG. 6. Neutron diffraction scans along the $[0 0 \ell]$ direction through the (222) reflection for $[\text{Fe}_3\text{O}_4(15 \text{ \AA})|\text{NiO}(70 \text{ \AA})]_{96}$ at 20 K, $[\text{Fe}_3\text{O}_4(34 \text{ \AA})|\text{NiO}(68 \text{ \AA})]_{300}$ at 10 K, $[\text{Fe}_3\text{O}_4(67 \text{ \AA})|\text{NiO}(33 \text{ \AA})]_{400}$ at 20 K, and $[\text{Fe}_3\text{O}_4(75 \text{ \AA})|\text{NiO}(9 \text{ \AA})]_{500}$ at 80 K. The scans are vertically offset for clarity and scaled by the MgO peak intensity. The solid lines represent fits to Gaussians.

interlayers, as expected from the structure-factor calculations. Growth-axis scans through the (220) peak are plotted in Fig. 7 for $[\text{Fe}_3\text{O}_4(34 \text{ \AA})|\text{NiO}(68 \text{ \AA})]_{300}$, $[\text{Fe}_3\text{O}_4(75 \text{ \AA})|\text{NiO}(9 \text{ \AA})]_{500}$ and the 3- μm -thick Fe_3O_4 film. The intensities have been scaled to illustrate the evolution of the peak shape with increasing NiO layer thickness. The reflection for the thick Fe_3O_4 film is a resolution-limited Gaussian indicative of long-range magnetic and crystalline order, while the reflection for $[\text{Fe}_3\text{O}_4(34 \text{ \AA})|\text{NiO}(68 \text{ \AA})]_{300}$ is broadened by a random distribution of interfacial stacking faults (FWHM = $2\pi/52 = 0.124 \text{ \AA}^{-1}$), as discussed in Sec. IV. [We note that the (220) peak for $[\text{Fe}_3\text{O}_4(67 \text{ \AA})|\text{NiO}(33 \text{ \AA})]_{400}$ is similar to that for $[\text{Fe}_3\text{O}_4(34 \text{ \AA})|\text{NiO}(68 \text{ \AA})]_{300}$ with a FWHM of 0.095 \AA^{-1} (i.e., $2\pi/69$). The (220) reflection for $[\text{Fe}_3\text{O}_4(68 \text{ \AA})|\text{NiO}(17 \text{ \AA})]_{100}$ has a FWHM of 0.088 \AA^{-1} (i.e., $2\pi/74$), but the peak for $[\text{Fe}_3\text{O}_4(15 \text{ \AA})|\text{NiO}(70 \text{ \AA})]_{96}$, with an expected FWHM of 0.42 \AA^{-1} (i.e., $2\pi/15$), is masked by the background.] For $[\text{Fe}_3\text{O}_4(75 \text{ \AA})|\text{NiO}(9 \text{ \AA})]_{500}$, however, the reflection fits to a Lorentzian with a FWHM of 0.022 \AA^{-1} , corresponding to a coherence length greater than 500 \AA . To determine the origin of this line shape, we have computed the (220) scattering cross section from Eq. (9) for a superlattice of comparable dimensions and determined that the peak changes smoothly from a narrow to a broad Gaussian as interfacial defects are introduced. [At the (220) position, we note that configuration (a) in Fig. 4 is indistinguishable from (c), and that (b) is indistinguishable from (d).] Lorentzian “wings” emerge as the defect population is increased to approximately 10%. We suggest that the

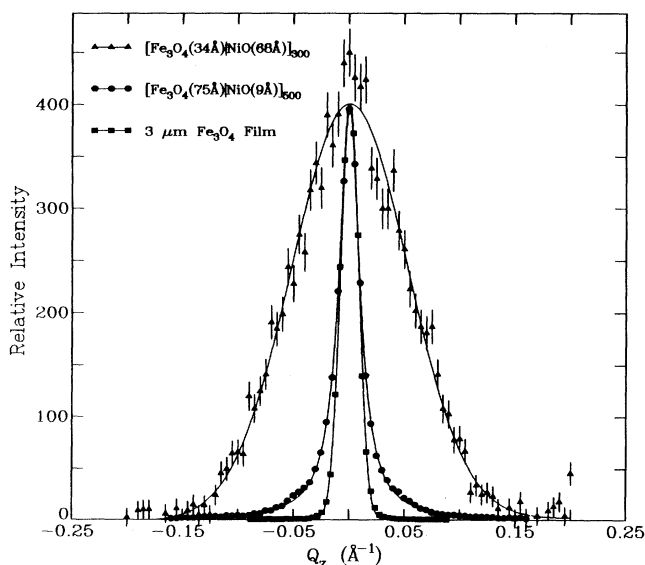


FIG. 7. Neutron diffraction scans along the $[0 \ 0 \ l]$ direction through the (220) reflection at 9 K for $[\text{Fe}_3\text{O}_4(34 \text{ \AA})|\text{NiO}(68 \text{ \AA})]_{300}$ (triangles) and 20 K for $[\text{Fe}_3\text{O}_4(75 \text{ \AA})|\text{NiO}(9 \text{ \AA})]_{500}$ (circles) and a 3- μm -thick Fe_3O_4 film (squares). The backgrounds have been subtracted from the data and the peak intensities have been normalized to a value of 400 counts to emphasize the peak-shape variations.

Fe_3O_4 lattice in a real sample is likely to retain its registry across thin NiO interlayers ($\lesssim 15 \text{ \AA}$) because Fe may be dispersed through the NiO (Fig. 2). The nominal NiO layer in $[\text{Fe}_3\text{O}_4(75 \text{ \AA})|\text{NiO}(9 \text{ \AA})]_{500}$ may partially tend toward the mixed spinel NiFe_2O_4 , which is ferrimagnetic.

Additional characterization of the crystalline and magnetic order within the Fe_3O_4 interlayers is provided by scans of the (220) peak along the $[l \ l \ 0]$ wave vector direction. From the FWHM of this in-plane reflection, we can estimate the magnetic and structural Fe_3O_4 coherence length *within* the growth plane of the superlattices. For samples with NiO layer thicknesses greater than 15 \AA , $[\text{Fe}_3\text{O}_4(34 \text{ \AA})|\text{NiO}(68 \text{ \AA})]_{300}$, $[\text{Fe}_3\text{O}_4(67 \text{ \AA})|\text{NiO}(33 \text{ \AA})]_{400}$, and $[\text{Fe}_3\text{O}_4(68 \text{ \AA})|\text{NiO}(17 \text{ \AA})]_{100}$, the extracted coherence length is approximately 160 \AA implying the presence of small in-plane domains. The (220) peaks for $[\text{Fe}_3\text{O}_4(75 \text{ \AA})|\text{NiO}(9 \text{ \AA})]_{500}$ and the 3- μm Fe_3O_4 film are resolution limited. Their in-plane coherence lengths clearly exceed 500 \AA . Because only the superlattice free of growth-axis defects has large in-plane domains, we suggest that the formation of stacking faults at the superlattice interfaces also induces significant structural and magnetic disorder across the sample face.

The integrated intensities of the (220) reflections in Fig. 7 decrease by less than 10% as the temperature is raised from 10 K to 700 K. Unfortunately, temperatures approaching the 858 K magnetic transition for bulk Fe_3O_4 are inaccessible because the crystalline structure of the samples degrades irreversibly upon annealing above $\approx 725 \text{ K}$.²⁹ Complementary magnetic hysteresis measurements confirm, however, that the ferrimagnetic Fe_3O_4 order persists and remains stable well above $T_N = 520 \text{ K}$ for bulk NiO.

Though the (111) reflection is comprised of magnetic scattering from both of the superlattice constituents (Table I), the pronounced temperature dependence of this peak originates solely from the spins in the NiO interlayers. Examples of growth-axis scans through the (111) reflection are plotted in Fig. 8 for $[\text{Fe}_3\text{O}_4(67 \text{ \AA})|\text{NiO}(33 \text{ \AA})]_{400}$ and $[\text{Fe}_3\text{O}_4(75 \text{ \AA})|\text{NiO}(9 \text{ \AA})]_{500}$. The peak for the first sample has two distinct components: a narrow Gaussian that gradually disappears with increasing temperature, and a broad Gaussian that exhibits little temperature dependence. Because this line shape resembles that of the (111) model calculation in Fig. 5, we identify the former component with NiO antiferromagnetic order coherent through three or more bilayers, and the latter with Fe_3O_4 ferrimagnetic order confined to a single bilayer by interfacial stacking faults. The superlattice sidebands apparent in the theoretical curve, however, are clearly not evident in the experimental data. In the model calculation, the magnitude of these peaks can be reduced relative to the central Bragg reflection by biasing the distribution of the interfacial stacking-faults toward configurations (a) and (b) in Fig. 4. [At the (111) position, the structure factors for interfaces (a) and (d) are indistinguishable, as are those for (b) and (c).] Data for $[\text{Fe}_3\text{O}_4(34 \text{ \AA})|\text{NiO}(68 \text{ \AA})]_{300}$ are similar to those in Fig. 8(a), implying a slight preference for selected inter-

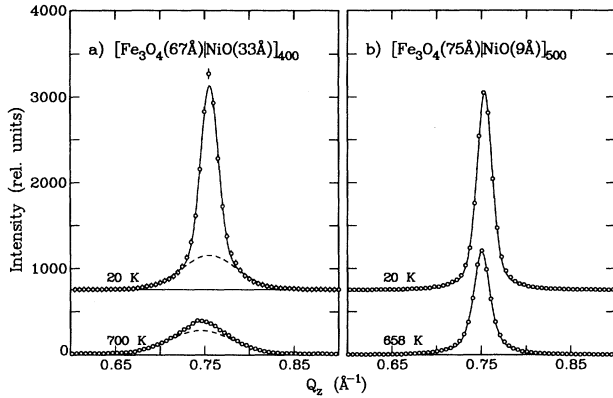


FIG. 8. Neutron diffraction scans along the $[0\ 0\ l]$ direction through the (111) reflection for $[\text{Fe}_3\text{O}_4(67\ \text{\AA})|\text{NiO}(33\ \text{\AA})]_{400}$ at 20 K and 700 K and for $[\text{Fe}_3\text{O}_4(75\ \text{\AA})|\text{NiO}(9\ \text{\AA})]_{500}$ at 20 K and 658 K. For the former, the broad Gaussian component (dashed line) corresponds to scattering from the Fe_3O_4 interlayers and the narrow Gaussian component results from the NiO interlayers.

face orientations in this sample as well. We also observe that the integrated intensities of the broad and narrow components scale roughly with the relative composition of the superlattice bilayer, leaving only the sharp Gaussian from the NiO for $[\text{Fe}_3\text{O}_4(15\ \text{\AA})|\text{NiO}(70\ \text{\AA})]_{96}$.

In contrast, the (111) scattering for $[\text{Fe}_3\text{O}_4(75\ \text{\AA})|\text{NiO}(9\ \text{\AA})]_{500}$ in Fig. 8(b) is better described by a single, resolution-limited peak with Lorentzian tails. Structure-factor calculations from Eq. (9) for a sample of similar dimensions reveal that this line shape evolves from a broad Gaussian as the population of interfacial stacking faults is decreased below 10%, corroborating results from the (220) data analysis. While the scattering contributions from the NiO and Fe_3O_4 magnetic order cannot be easily separated for this sample, the striking temperature dependence of this reflection clearly tracks the decay of the antiferromagnetic order in the thin NiO interlayers.

VI. NICKEL-OXIDE MAGNETIC ORDER

Taking advantage of the disparate length scales of the NiO and Fe_3O_4 crystalline coherence, we can monitor separately the order parameters for the Fe and Ni moments. In Fig. 9 the integrated intensity of the (111) peak scanned along the $[l\ l\ l]$ direction is plotted as a function of temperature for $[\text{Fe}_3\text{O}_4(67\ \text{\AA})|\text{NiO}(33\ \text{\AA})]_{400}$, $[\text{Fe}_3\text{O}_4(34\ \text{\AA})|\text{NiO}(68\ \text{\AA})]_{300}$, $[\text{Fe}_3\text{O}_4(15\ \text{\AA})|\text{NiO}(70\ \text{\AA})]_{96}$, and the $1\text{-}\mu\text{m}$ -thick NiO film. (For the first two samples the contribution from the Fe_3O_4 interlayers has been subtracted.) This intensity, which is proportional to the square of the Ni moment, decreases smoothly with increasing temperature following the behavior of a classical antiferromagnet. For both $[\text{Fe}_3\text{O}_4(15\ \text{\AA})|\text{NiO}(70\ \text{\AA})]_{96}$ and the NiO film, the order parameter approaches zero near 520 K, the Néel temperature for bulk NiO. In contrast, the (111) NiO intensity levels off near 600 K for

$[\text{Fe}_3\text{O}_4(34\ \text{\AA})|\text{NiO}(68\ \text{\AA})]_{300}$, but continues to decline above 700 K for both $[\text{Fe}_3\text{O}_4(67\ \text{\AA})|\text{NiO}(33\ \text{\AA})]_{400}$ and $[\text{Fe}_3\text{O}_4(75\ \text{\AA})|\text{NiO}(9\ \text{\AA})]_{500}$. Recall that the Fe_3O_4 intensity at the (111) position remains constant even above the temperature at which the sharp NiO component disappears [Fig. 8(a)]. In all four of the superlattices the Ni and Fe moments thus appear to order at separate temperatures, but the Néel temperature for the former shifts systematically toward that of bulk Fe_3O_4 as the relative NiO thickness is decreased. Magnetic order is apparently induced in the NiO interlayers above the bulk ordering temperature due to the proximity of the ferrimagnetic Fe_3O_4 interlayers.

Mean-field theory demonstrates that the observed scaling of the NiO transition temperature is a natural consequence of the short-range interlayer exchange coupling. This treatment was originally developed to describe similar behavior in antiferromagnetic NiO/CoO (Refs. 3 and 11) and $\text{FeF}_2/\text{MnF}_2$ (Refs. 9 and 10) superlattices. We have modified the formalism to reflect differences between the nature of the magnetic ordering in the Fe_3O_4 and NiO interlayers. The problem is simplified considerably by approximating the superlattice as a structure with ferromagnetic rows of spins coupled antiferromagnetically along the modulation direction. To simulate the ferrimagnetic spin arrangement of the Fe_3O_4 , the density of spins in alternating Fe layers is set equal to half that in the Ni layers, as schematically depicted in the inset of

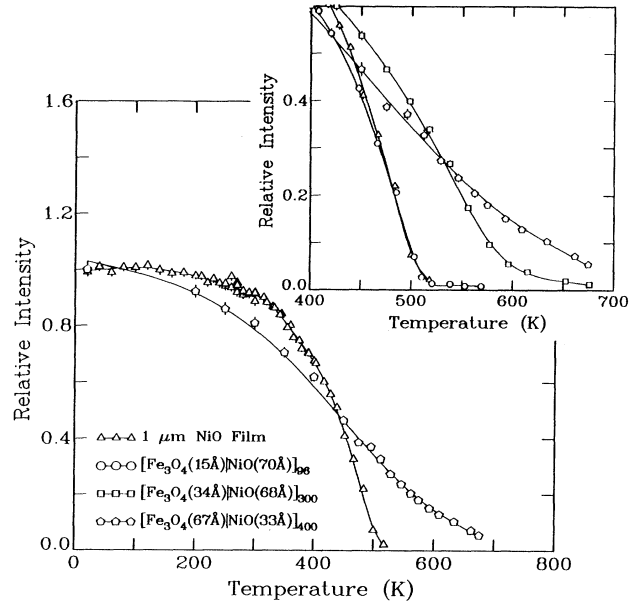


FIG. 9. Temperature dependence of the integrated intensity of the (111) peak scanned along the $[l\ l\ l]$ direction plotted for $[\text{Fe}_3\text{O}_4(67\ \text{\AA})|\text{NiO}(33\ \text{\AA})]_{400}$ (pentagons) and the $1\text{-}\mu\text{m}$ -thick NiO film (triangles). The inset shows the order parameters near the NiO phase transition for these two samples, as well as $[\text{Fe}_3\text{O}_4(15\ \text{\AA})|\text{NiO}(70\ \text{\AA})]_{96}$ (circles) and $[\text{Fe}_3\text{O}_4(34\ \text{\AA})|\text{NiO}(68\ \text{\AA})]_{300}$ (squares). The portion of the intensity originating from the Fe_3O_4 has been subtracted as background. For all four samples, the intensities have been scaled by their low-temperature saturation values.

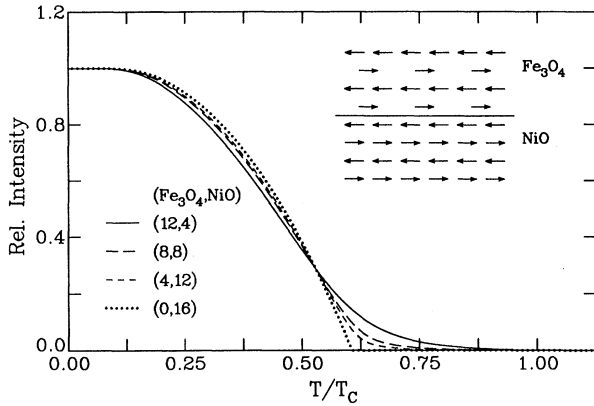


FIG. 10. Temperature dependence of the square of the average Ni moment through a single NiO interlayer calculated from the mean-field treatment described in the text for bilayers with $(N_{\text{Fe}_3\text{O}_4}, N_{\text{NiO}}) = (12,4)$ (8,8), (4,12), and (0,16) corresponding to the solid, long-dashed, short-dashed, and dotted lines, respectively. The moments have been scaled by their low-temperature saturation values, and the temperature is scaled by T_C for bulk Fe_3O_4 . The inset shows a schematic of the simplified bilayer structure used for the mean-field calculation.

Fig. 10. The profile of the spin structure through a single bilayer with $N_{\text{Fe}_3\text{O}_4}$ atomic layers of Fe_3O_4 and N_{NiO} layers of NiO is then extracted from a self-consistent solution of the Brillouin function \mathcal{B}_S .³⁰ The effective molecular field includes only the nearest-neighbor interactions between the rows. For the i th plane in the bilayer,

$$\langle S_i \rangle = \mathcal{B}_S \left(\frac{\mathcal{J}_i Z_{i-1} \langle S_{i-1} \rangle + \mathcal{J}_i Z_{i+1} \langle S_{i+1} \rangle}{k_B T} \right), \quad (10)$$

where $\langle S_i \rangle$ represents the thermal average of the spins in the i th layer and Z_{i-1} is the coordination number between spins in the i th and $i-1$ st row. The antiferromagnetic exchange parameters, $\mathcal{J}_{\text{Fe}_3\text{O}_4}$ and \mathcal{J}_{NiO} , are determined from the Néel temperatures for bulk Fe_3O_4 and NiO, respectively. The $\text{Fe}_3\text{O}_4/\text{NiO}$ interface is restricted to a single atomic layer with \mathcal{J}_i equal to the average of these two parameters. For the purposes of the model, $S_{\text{Fe}} = 4.5$ for the Fe ions at both the tetrahedral and octahedral sites, and $S_{\text{Ni}} = 1.5$.

Figure 10 shows the square of the average Ni moment through a single NiO interlayer plotted as a function of temperature for four bilayers with $(N_{\text{Fe}_3\text{O}_4}, N_{\text{NiO}}) = (12,4)$, (8,8), (4,12), and (0,16). These calculated curves qualitatively resemble the diffraction data in Fig. 9 throughout the entire temperature range, but the repeat distance of the hypothetical bilayers (≈ 40 Å) is less than half that of the actual samples. In the model, the Fe_3O_4 and NiO interlayers develop finite moments at distinct temperatures. While the Fe_3O_4 transition temperature does not deviate significantly from that of bulk, the apparent ordering temperature for the NiO exhibits a pronounced dependence on the relative composition of the bilayer, as is experimentally observed. The mean-field treatment even duplicates the “tail” that emerges

at high temperatures for samples with thin NiO interlayers. Similar calculations for a series of bilayers with constant $N_{\text{Fe}_3\text{O}_4} = 8$ suggest that the calculated NiO ordering temperature is more sensitive to the NiO layer thickness than to the Fe_3O_4 thickness. Increasing the bilayer repeat distance in this mean-field approximation to realistic values, however, merely drives the apparent ordering temperatures for the NiO and Fe_3O_4 layers closer to their bulk values.

Though this mean-field theory is too simplistic for a direct comparison with the experimental results, it does clearly demonstrate that the exchange coupling of the NiO and Fe_3O_4 spins across the superlattice interfaces is principally responsible for the observed enhancement of the NiO ordering temperature. Limitations are imposed by the use of a two-dimensional model for the magnetic structure (inset of Fig. 10) rather than a three-dimensional description of the actual NiO and Fe_3O_4 spin structures. The quantitative agreement with experiment could also be improved by including the effects of interfacial mixing, which may account for the bulklike Néel temperature observed for $[\text{Fe}_3\text{O}_4(15 \text{ Å})|\text{NiO}(70 \text{ Å})]_{96}$ (Fig. 9), and competing anisotropies, which modify the bulk magnetic behavior as discussed in the following section.

VII. IRON-OXIDE MAGNETIC ORDER

For an ideal $\text{Fe}_3\text{O}_4/\text{NiO}$ superlattice, mean-field analysis also predicts that the high-temperature anomaly associated with the Fe_3O_4 phase transition actually marks the onset of long-range magnetic order through the entire bilayer.⁹ Even in samples with thick NiO interlayers, an infinitesimal moment should persist on the Ni sites well above their apparent ordering temperature. In reality the Fe order may, in fact, be confined to a single Fe_3O_4 interlayer at these temperatures due to thermal fluctuations, structural defects, or other sources of disorder. Polarized beam measurements of the (220) and (111) reflections for $[\text{Fe}_3\text{O}_4(34 \text{ Å})|\text{NiO}(68 \text{ Å})]_{300}$ and $[\text{Fe}_3\text{O}_4(67 \text{ Å})|\text{NiO}(33 \text{ Å})]_{400}$ show no change in the ferrimagnetic magnetization of the Fe_3O_4 layers upon heating to 700 K. Because the magnetic coherence, as calculated from peak width measurements, is restricted by the structural stacking faults at the superlattice interfaces, we cannot directly determine if the Fe layers couple across the NiO interlayers at high temperatures.

Bulk magnetization studies, however, indicate that the nature of the interlayer interaction differs substantially above and below the Néel temperature for bulk NiO in samples with thick NiO interlayers ($\gtrsim 15\text{--}20$ Å). For example, the in-plane hysteresis profile for a superlattice with 17 Å of Fe_3O_4 and 17 Å of NiO is nearly linear at 30 K, but gradually returns to a sigmoidal shape similar to bulk Fe_3O_4 as the temperature is raised above ≈ 520 K.²⁹ Exchange coupling of the Fe and Ni spins at the superlattice interfaces apparently frustrates the ferrimagnetic ordering at low temperatures. The strength of this interaction decreases significantly at high temperatures, allowing the Fe_3O_4 interlayers to order independently. In

contrast, the hysteresis loops for superlattices with NiO interlayer thicknesses $\lesssim 15$ Å are linear over an extended temperature range, possibly as a result of the bridging of the Fe_3O_4 layers across the NiO (e.g., Fig. 2). The NiO thickness dependence of this coupling between the Fe_3O_4 layers has also been observed using ferromagnetic resonance (FMR) techniques.³¹ With the exception of samples with the thinnest NiO interlayers, the temperature dependence of the magnetization follows the softening of the NiO anisotropy which occurs near the Néel transition for the NiO component.

Neutron diffraction analysis at temperatures well below 520 K also reveals that the anisotropy of the Fe_3O_4 is altered by interfacial coupling to the NiO or demagnetizing effects. Polarized neutron experiments suggest that the distribution of the Fe moments among equivalent axial domains is roughly uniform in zero field, with a slight preference for alignment in the growth plane. Specifically, the flipping ratio³² of the (220) reflection was measured for $[\text{Fe}_3\text{O}_4(67 \text{ Å})|\text{NiO}(33 \text{ Å})]_{400}$, $[\text{Fe}_3\text{O}_4(75 \text{ Å})|\text{NiO}(9 \text{ Å})]_{500}$ and the 3 μm Fe_3O_4 film with the neutrons polarized both parallel and perpendicular to the scattering vector in order to separate the magnetic scattering contributions from the structural. Unfortunately, this analysis is not sensitive to the moment orientation within the plane.

A direct comparison of the magnetic hysteresis profiles for the superlattices considered elucidates the dependence of the Fe anisotropy on the relative Fe_3O_4 and NiO layer thicknesses. The field-dependent magnetization is plotted in Fig. 11 for $[\text{Fe}_3\text{O}_4(15 \text{ Å})|\text{NiO}(70 \text{ Å})]_{96}$, $[\text{Fe}_3\text{O}_4(67 \text{ Å})|\text{NiO}(33 \text{ Å})]_{400}$, and $[\text{Fe}_3\text{O}_4(75 \text{ Å})|\text{NiO}(9 \text{ Å})]_{500}$ at 300 K for a field applied along a [100] axis in the growth plane. The hysteresis curve for $[\text{Fe}_3\text{O}_4(75 \text{ Å})|\text{NiO}(9 \text{ Å})]_{500}$ resembles that of bulk because the chemical interfacial “mixing”

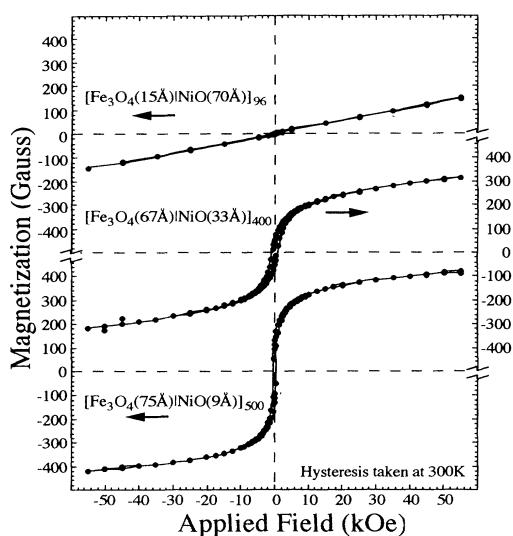


FIG. 11. Magnetization at 300 K as a function of field applied along a [100] direction in the growth plane for $[\text{Fe}_3\text{O}_4(15 \text{ Å})|\text{NiO}(70 \text{ Å})]_{96}$, $[\text{Fe}_3\text{O}_4(67 \text{ Å})|\text{NiO}(33 \text{ Å})]_{400}$, and $[\text{Fe}_3\text{O}_4(75 \text{ Å})|\text{NiO}(9 \text{ Å})]_{500}$.

(refer to Fig. 2) promotes a direct interaction between the Fe_3O_4 interlayers. As the relative NiO thickness is increased, the loop flattens until it becomes nearly linear, suggesting a biasing of the Fe_3O_4 anisotropy energy toward that of bulk NiO. Supplementary magnetization measurements on related samples indicate that the Fe anisotropy energy is significantly enhanced in samples with Fe_3O_4 thicknesses less than 34 Å, regardless of the NiO interlayer thickness.⁸ We suggest that the Fe moments in these samples are completely pinned to the direction of the Ni moments in adjacent interlayers.

We note that the Fe_3O_4 anisotropy is also dependent on temperature. The easy-axis of magnetization changes near the 120 K Verwey transition, but only in samples with thick Fe_3O_4 interlayers.^{7,29} In supplementary neutron diffraction measurements of the superlattices described here, we observe that the $(4 \ 0 \ \frac{1}{2})$ peak, characteristic of the distorted structural phase below T_V , is evident only for $[\text{Fe}_3\text{O}_4(75 \text{ Å})|\text{NiO}(9 \text{ Å})]_{500}$ and the 3- μm Fe_3O_4 film.³³ We believe that the suppression of this transition in the remaining samples results principally from clamping of the accompanying Fe_3O_4 lattice distortion by epitaxial constraints, rather than from stoichiometry variations within the Fe_3O_4 interlayers. To aid in the separation of these two effects in superlattices, systematic studies of the Verwey transition in a series of thick $\text{Fe}_3\text{O}_{4-\delta}$ films with $0 < \delta < 1$ have been performed and are detailed elsewhere.³⁴

VIII. CONCLUSION

Neutron diffraction measurements of $\text{Fe}_3\text{O}_4/\text{NiO}$ superlattices reveal that the NiO antiferromagnetic order is long range at low temperatures, despite the contrasting magnetic structures of the component materials. In samples with thick NiO interlayers, however, stacking faults at the superlattice interfaces restrict both the structural and magnetic coherence of the ferrimagnetic Fe_3O_4 to the width of a single interlayer. Specifically, the orientation of the Fe_3O_4 spinel unit cell relative to the NiO rocksalt template is not uniquely defined in the [001] growth plane. We have identified the types of interfacial defects possible in these samples and incorporated them into a model for the structure factor based upon the Hendricks-Teller formalism for structural disorder.¹⁸ The model qualitatively reproduces anomalous features of the diffraction data such as the broadening of the (220) reflection and the two-component line shape of the (111) peak.

In addition, we have demonstrated that the scattering contributions from the Fe and Ni moments can easily be separated within the framework of this model. For the four superlattices considered, the phase transition temperatures for the Fe_3O_4 and NiO interlayers appear to be distinct. While the ordering temperature of the Fe_3O_4 tends toward its bulk value (858 K), the Néel temperature for the NiO varies between its bulk value (520 K) and that of Fe_3O_4 as the relative NiO thickness is decreased. The scaling of the NiO transition temperature loosely follows the predictions of a mean-field theory for

a superlattice composed of antiferromagnetic and ferromagnetic interlayers.

A comparison of the neutron diffraction results with complementary magnetization measurements clearly indicates that the modified magnetic behavior of the Fe_3O_4 and NiO interlayers originates from the exchange coupling of the two materials at the superlattice interfaces. It is surprising that this coupling alters the magnetic behavior of interlayers thicker than 70 Å, a length scale much larger than that expected from mean-field analy-

sis. The exact nature of the exchange interaction in this system remains a topic for future study.

ACKNOWLEDGMENTS

We thank M. J. Carey and C. F. Majkrzak for helpful discussions and insights. The work at FSU was supported through the National Science Foundation under Grant No. DMR-92-6870 and Grant No. N00014-92-J-1356 from Office of Naval Research.

- ¹ L.M. Falicov, Daniel T. Pierce, S.D. Bader, R. Gronsky, Kristl B. Hathaway, Herbert J. Hopster, David N. Lambeth, S.S.P. Parkin, Gary Prinz, Myron Salamon, Ivan K. Schuller, and R.H. Victora, *J. Mater. Res.* **5**, 1299 (1990).
- ² C.A. Ramos, D. Lederman, A.R. King, and V. Jaccarino, *Phys. Rev. Lett.* **65**, 2913 (1990).
- ³ J.A. Borchers, M.J. Carey, R.W. Erwin, C.F. Majkrzak, and A.E. Berkowitz, *Phys. Rev. Lett.* **70**, 1878 (1993); J.A. Borchers, M.J. Carey, A.E. Berkowitz, R.W. Erwin, and C.F. Majkrzak, *J. Appl. Phys.* **73**, 6898 (1993).
- ⁴ Y. Bando, M. Takano, T. Terashima, and Z. Hiroi, *MRS Int'l. Mtg. Adv. Mats.* **10**, 83 (1989); M. Takano, T. Terashima, and Y. Bando, *Appl. Phys. Lett.* **51**, 205 (1987).
- ⁵ D.M. Lind, S.D. Berry, G. Chern, H. Mathias, and L.R. Testardi, *Phys. Rev. B* **45**, 1838 (1992); *J. Appl. Phys.* **70**, 6218 (1991).
- ⁶ J.A. Borchers, R.W. Erwin, S.D. Berry, D.M. Lind, E. Lochner, and K.A. Shaw, *Appl. Phys. Lett.* **64**, 381 (1994); Eq. (2) in this article was misprinted. It should have the form of Eq. (9) in the current text.
- ⁷ D.M. Lind, S.-P. Tay, S.D. Berry, J.A. Borchers, and R.W. Erwin, *J. Appl. Phys.* **73**, 6886 (1993).
- ⁸ S.D. Berry, D.M. Lind, E. Lochner, K.A. Shaw, D. Hilton, R.W. Erwin, and J.A. Borchers, in *Magnetic Ultrathin Films*, edited by B.T. Jonker, Takeshi Egami, Scott A. Chambers, P. Grünberg, R.F.C. Farrow, Kannan M. Krishnan, C. Chappert, Ernesto E. Marinero, R. Clarke, Carl Rau, W.J.M. de Jonge, and Shigeru Tsunashima, *MRS Symposia Proceedings No. 313* (Materials Research Society, Pittsburgh, 1993), p. 779.
- ⁹ R.W. Wang and D.L. Mills, *Phys. Rev. B* **46**, 11 681 (1992).
- ¹⁰ A.S. Carrico and R.E. Camley, *Phys. Rev. B* **45**, 13 117 (1992).
- ¹¹ Shufeng Zhang and Guihua Zhang, *J. Appl. Phys.* **75**, 6685 (1994).
- ¹² H.T. Diep, *Phys. Rev. B* **40**, 4818 (1989).
- ¹³ D. Lederman, D.P. Belanger, J. Wang, S.J. Han, C. Paduani, C.A. Ramos, and R.M. Nicklow, in *Magnetic Ultrathin Films*, edited by B.T. Jonker, Takeshi Egami, Scott A. Chambers, P. Grünberg, R.F.C. Farrow, Kannan M. Krishnan, C. Chappert, Ernesto E. Marinero, R. Clarke, Carl Rau, W.J.M. de Jonge, and Shigeru Tsunashima (Ref. 8), p. 333.
- ¹⁴ M.J. Carey, A.E. Berkowitz, J.A. Borchers, and R.W. Erwin, *Phys. Rev. B* **47**, 9952 (1993); M.J. Carey and A.E. Berkowitz, *J. Appl. Phys.* **73**, 6892 (1993).
- ¹⁵ W.L. Roth, *J. Appl. Phys.* **31**, 2000 (1960).
- ¹⁶ C.G. Shull, E.O. Wollan, and W.C. Koehler, *Phys. Rev.* **84**, 912 (1951); Walter C. Hamilton, *ibid.* **110**, 1050 (1958); K.J. Standley, *Oxide Magnetic Materials* (Oxford University, London, 1972), p. 23f.
- ¹⁷ M. Iizumi, T.F. Koetzle, G. Shirane, S. Chikazumi, M. Matsui, and S. Todo, *Acta. Crystallogr. B* **38**, 2121 (1982); Soshin Chikazumi, *Physics of Magnetism* (Wiley, New York, 1964), p. 387, and references therein.
- ¹⁸ Sterling Hendricks and Edward Teller, *J. Chem. Phys.* **10**, 147 (1942).
- ¹⁹ This and all subsequent diffraction peaks discussed here are indexed with respect to the Fe_3O_4 spinel unit cell and NiO magnetic unit cell.
- ²⁰ E.E. Fullerton, I.K. Schuller, H. Vanderstraeten, and Y. Bruynseraede, *Phys. Rev. B* **45**, 9292 (1992).
- ²¹ J.F. Ankner, J.A. Borchers, R.F.C. Farrow, and R.F. Marks, *J. Appl. Phys.* **73**, 6427 (1993).
- ²² J.F. Ankner and C.F. Majkrzak, *SPIE Conf. Proc.* **1738**, 260 (1992).
- ²³ A.P. Payne and B.M. Clemens, *Phys. Rev. B* **47**, 2289 (1993).
- ²⁴ R.W. Erwin, J.J. Rhyne, M.B. Salamon, J. Borchers, Shantanu Sinha, R. Du, J.E. Cunningham, and C.P. Flynn, *Phys. Rev. B* **35**, 6808 (1987).
- ²⁵ G.E. Bacon, *Neutron Diffraction* (Clarendon, Oxford, 1975), p. 226f.
- ²⁶ Par J. Méring, *Acta. Crystallogr.* **2**, 371 (1949).
- ²⁷ Jiro Kakinoki and Yukitomo Komura, *J. Phys. Soc. Jpn.* **7**, 30 (1952); Equation (27) in this work is identical to Eq. (9) in the current text.
- ²⁸ Because the repeat length of the NiO magnetic structure along the growth direction equals the lattice constant a , it is necessary in this construction to constrain Λ to be an integer multiple of a in order to preserve the integrity of the Hendricks-Teller formalism for one bilayer relative to the next.
- ²⁹ S.D. Berry, D.M. Lind, G. Chern, and H. Mathias, *J. Magn. Mater.* **123**, 126 (1993).
- ³⁰ J. Samuel Smart, *Effective Field Theories of Magnetism* (W.B. Saunders, Co., Philadelphia, 1966), pp. 6 and 113f.
- ³¹ J.J. Krebs, D.M. Lind, and S.D. Berry, *J. Appl. Phys.* **73**, 6457 (1993).
- ³² The "flipping ratio" corresponds to the ratio of the non-spin-flip scattering to the spin-flip scattering. For a general discussion of polarized neutron diffraction, refer to R.M. Moon, T. Riste, and W.C. Koehler, *Phys. Rev.* **181**, 920 (1969).
- ³³ D.M. Lind, J.A. Borchers, R.W. Erwin, J.F. Ankner, E. Lochner, K.A. Shaw, R.C. DiBari, W. Portwine, P. Stoyanov, and S.D. Berry, *J. Appl. Phys.* **76**, 6284 (1994); D.M. Lind, S.D. Berry, J.A. Borchers, R.W. Erwin, E. Lochner, and K.A. Shaw (unpublished).
- ³⁴ E. Lochner, K.A. Shaw, R.C. DiBari, W. Portwine, P. Stoyanov, S.D. Berry, and D.M. Lind, *IEEE Trans. Magn.* **30**, 4912 (1994).

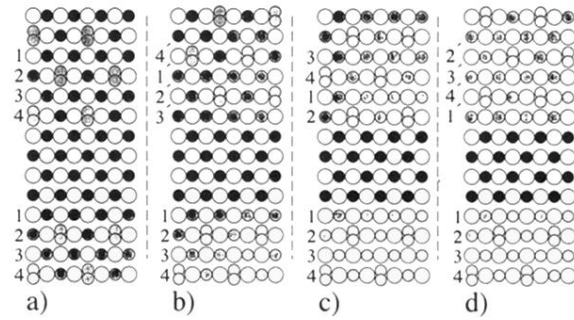


FIG. 4. Projection of a $\text{Fe}_3\text{O}_4/\text{NiO}$ interface in the y - z plane. Schematics (a)–(d) show the four possible orientations of the Fe_3O_4 -spinel lattice relative to the NiO -rocksalt lattice at each interface. (For clarity, the interfaces shown are not diffused or mixed, as may be the case in an actual superlattice.) The open circles represent the O^{+2} ions, the solid circles correspond to the Ni^{+2} ions, the shaded circles designate the Fe^{+2} and Fe^{+3} ions occupying the tetrahedral and octahedral sites. Symmetrically equivalent atomic planes in the spinel unit cell are numbered 1–4 in each interfacial configuration.